Online ISSN 1848-3380, Print ISSN 0005-1144
ATKAFF 56(4), 508–521(2015)

José-Joel Gonzalez-Barbosa, José-Guadalupe Rico-Espino, Roberto-Augusto Gómez-Loenzo,Hugo Jiménez-Hernández, Miguel Razo, Ricardo Gonzalez-Barbosa

Accurate 3D Reconstruction using a Turntable-based and Telecentric Vision

DOI 10.7305/automatika.2016.01.1033
UDK 621.375.826:004.514.66

Original scientific paper

This paper presents a camera+telecentric lens that is able to obtain 3D information. We designed and implemented a method which can register and integrate 3D information captured from different viewpoints to build a complete 3D object model. First, a geometric model of a camera+telecentric lens is established. Then a calibration process using a planar checkerboard is developed and implemented. The object is placed on a rotation stage in front of a stationary camera. Normally the rotation axis is considered to be aligned with camera frame. In the description presented in this paper, the rotation matrix and translation vector of the rotation axis are calibrated. At the same time, a three-dimensional reconstruction system based on contour extraction of objects with dimensions less than $50\ mm$ in diameter is developed. Finally, an analysis of the uncertainty model parameters and performance reconstruction of 3D objects are discussed.

Key words: Calibration, 3D Reconstruction, Telecentric lens

Točna 3D rekonstrukcija zasnovana na rotirajućoj platformi i telecentričnoj viziji. Članak prestavlja sustav koji se sastoji od kamere i telecentrične leće koji omogućavaju dobivanje 3D informacije o objektu. Dizajnirana je i implementirana metoda koja može registrirati i integrirati 3D informacije iz različitih točaka gledišta, kako bi se izgradio potpuni 3D model. Na početku, uspostavlja se geometrijski model kamere i telecentrične leće. Nakon toga koristi se razvijena metoda kalibracije zasnovana na šahovskoj ploči te se objekt postavlja na rotirajuću platformu ispred stacionarne kamere. Također, pretpostavlja se da je os rotacije poravnta s koordinantim sustavom kamere. U ovome članku kalibriraju se rotacijska matrica i translacijski vektor rotacijske osi. Razvijen je i sustav 3D rekonstrukcija zasnovan na izlučivanju kontura objekta dimenzija manjih od $50\ mm$ u promjeru. Na kraju, provedena je i analiza nesigurnosti parametara modela kao i točnost rekonstrukcije 3D modela.

Ključne riječi: kalibracija, 3D rekonstrukcija, telecentrična leća

1 INTRODUCTION

Three-dimensional reconstruction of small objects has become important [1–3]. Many interesting studies are related to small sized objects such as jewelry, coins, and miniature objects, which in most cases have been studied just to allow their virtual presentation. Recently, there is also an increasing number of applications related to material analysis and non-destructive analysis [1, 4].

The work presented in this paper is classified as an optical method, which relies on a digital camera and a telecentric lens to acquire images to be used in the three-dimensional reconstruction of objects. The optical system formed by a camera and a perspective lens is common, so this model and its calibration have been extensively studied. When the imaging conditions are limited to a few focal lengths from the object of interest the central perspective model introduces significant geometric and radiometric distortions [5, 6]. Since the system with camera and telecentric lens is a less-studied research topic, a calibration model that allows three-dimensional reconstruction of pieces with less than $50\ mm$ of diameter must be developed and implemented. In machine vision systems, telecentric lenses allow reducing some of the most common factors of image acquisition: the magnification changes, due to the position of the optical system and the object, image distortion, and perspective effects. Although high quality telecentric lenses normally show very low distortion degree, in the range of 0.1%, which seems to be very small, it would actually result into measurement errors approaching the size of one pixel of a camera [7]. This must not happen in precise measurement. In fact, errors such as radial distortion is inevitably in telecentric lenses system.

In previous work [8] a 3D reconstruction system is pre-

sented. The model used, is comprised by a telecentric lense and a rotation stage. Measurement validation is carried out using a digital caliper, an instrument that is not a conventional pattern calibration. The validation shown is for bidimensional vision systems, even though the instrument developed is a three-dimensional reconstruction systems, and the camera model and calibration does not consider radial distortion. Opto Engineering lenses exhibit a less than 0.1% radial distortion. Another important parameter to be minimized in this lens is trapezoidal distortion, however it is very difficult to calibrate by software [7]. An important assumption in that work, is that the rotation axis and camera frame are aligned; this is a strong assumption, because in order to match both frames, it is necessary to know physically the camera frame. In this work, we evaluate the 2D and 3D measurements using a plug gage. The plug gages are typically used as calibration patterns. For the 2D measurement, we take a set of points in an image. Then calculate the 2D position of each point in the world, taking into account lens radial distortion and camera's calibration parameters. Accuracy is obtained by measuring the discrepancy between the 2D points (obtained from the image projected to the world using the camera model) and the real 2D points that correspond to the plug gage measurement. The 3D measurement uses more than two images to reconstruct the complete object and the measurement is made to consider that the plug gage are cylinders. In addition, this work calibrates the rotational axis respect to the camera because mechanically is very difficult to make coincide the camera frame with respect to reference axis rotation.

The proposed solution for the 3D model reconstruction problem is illustrated in Figure 1. It consists in placing the object on the rotation stage, then multiple images are taken from different viewpoints while the stage rotates at known angles. The rotational axis of the rotational stage are not aligned to camera frame, the rotation matrix and translation vector of the rotation axis are calibrated using several images of a checkerboard pattern acquired at a known angle, at the same time, the intrinsic parameters are calculated. For each viewpoint, the contour object is extracted from the image and the contour dimensions are computed using the vision system calibration parameters. Using the rotation stage angle and the rotation axis, a complete 3D object shape is then obtained.

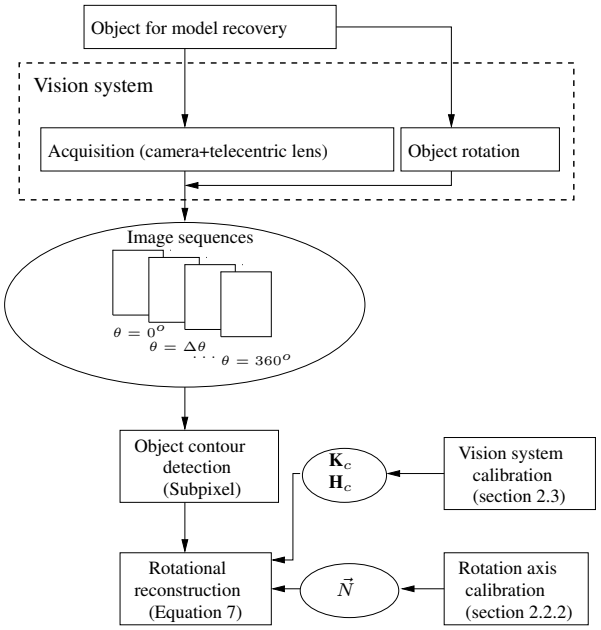

Fig. 1. System flow chart of a complete 3D model reconstruction.

2 METHODOLOGY

2.1 Overview

Three-dimensional reconstruction can be applied in several fields such as: manufacturing processes [9], metrology [10], robotics [11], biology [12], medicine [2, 13], topography [14], computer-aided design [15], archaeological [4], simulation [16] and scientific visualization [17] as examples. There are many techniques that have been successfully applied for the 3D reconstruction of small objects, such as laser scanners [3], X-ray Tomography [18], microscopy [1], which involves the use of expensive, but not very versatile equipment. Traditionally, coordinate measurement machines (CMMs) have been used for surface profile analysis [19]. This method is still extensively used in industries, although there are limitations such as low speed, high cost and disadvantages for applications that require fast measurements in soft materials.

The use of digital images represents a valid alternative, because a picture contains all the information needed to recover the object shape. Optical methods, such as interferometry [20], stereo vision [21–23], structured light projection [24, 25] and shape from focus/defocus [26–28] techniques, have long received extensive attention for reconstruction of 3D objects. Unlike CMM, measurement systems developed from optical principles are non-contact in nature, and consequently mechanical wear and surface deformation problems do not appear.

Two of the main features of these optical methods are high resolution and large measurement range. Measurement of millions of points can be accomplished within a few seconds. In [23], the authors describe a novel volumetric method for small objects. The authors use a binocular machine vision system composed of a camera+telecentric

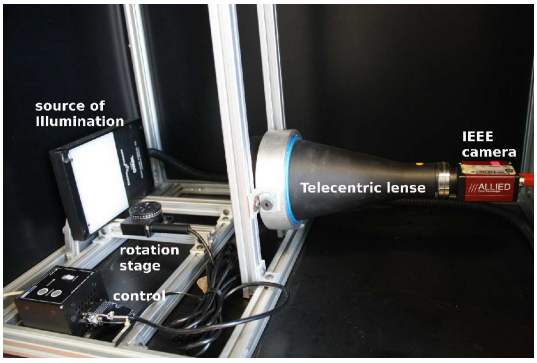

Fig. 2. The equipment hardware setup.

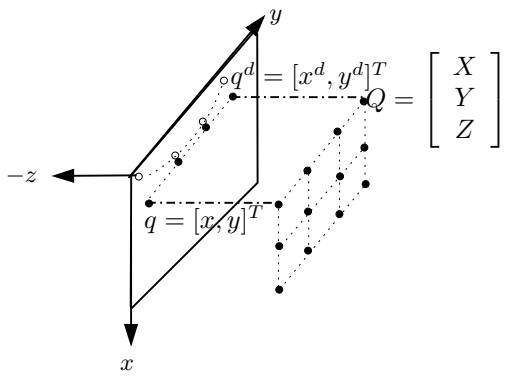

Fig. 3. Orthographic projection model of a real point (Q) onto the image plane (q). The point q corresponds to a perfect projection; whereas q^d represents the distorted point.

lens and an algorithm for calibration and 3D reconstruction, in which the calibration algorithm calculates the parameters incrementally. First the parameters for the camera model are computed, then using these values, distortion parameters are calculated, and finally, all the parameter values are refined by an iterative optimization algorithm. The 3D reconstruction is achieved by triangulation between shapes detected on two images by correspondence. In [29], the authors proposed a calibration method for the telecentric imaging system. They improved a two-step approach to accomplish the calibration, which consists of a telecentric lens camera model followed by a nonlinear refinement that considers the radial distortion. In [22] a shape representation for objects, which is based on 3D contour fragments and builds a 3D Contour Cloud, is described. The approach for the automatic reconstruction of such 3D Contour Clouds from calibrated stereo image sequences includes a novel idea that consists of a robust motion analysis. The stereo reconstruction is based on shape correspondences, in which the search space is limited to a subset of contours by only taking into account those contour fragments that lie in regions restricted by the epipolar lines. In [30], a combination of surface fitting and registration based on a squared distance minimization algorithm is discussed and applied to a constrained reverse engineering of CAD models.

2.2 Vision system model

The image sequence and the corresponding texture information are obtained by a vision system. It includes a digital camera with a telecentric lens, a motorized rotation stage, an illumination system, and a PC (Figure 2). The digital camera is a Marlin F-145 C model, the lens is a TC series bi-telecentric lenses of Opto Engineering [7], the motorized stage is a Thorlabs Z700 series, and the illumination is a Dolan-Jenner back lights model M1000.

In order to perform measurements, a mathematical relationship between the three-dimensional point Q and the image coordinates q must be established. To accomplish this, a precise model for the camera+telecentric lense system is developed. A calibration process is subsequently performed to obtain the parameters of the optical system model. The orthographic geometry, as illustrated in Figure 3, is the projection of a three-dimensional entity on a plane image by a set of parallel rays orthogonal to this plane. In Figure 3, we have that $x = X$, and $y = Y$, where (X, Y) and (x, y) denote the coordinates of the object and image respectively. The orthographic projection $q = [x, y, 1]^T$ of a point $Q = [X, Y, Z, 1]^T$ defined in world frame can be modeled by Equation 1.

$$q = \mathbf{KE}Q \tag{1}$$

$\mathbf{K}$ is defined as the intrinsic parameter matrix and $\mathbf{E}$ as the extrinsic parameters matrix, defined by Equation 2.

$$\mathbf{K}= \begin{bmatrix} \alpha & \gamma & 0 & 0 \\ 0 & \beta & 0 & 0 \\ 0 & 0 & 0 & 1 \end{bmatrix} ; \mathbf{E}= \begin{bmatrix} \mathbf{R} & \vec{T} \\ \mathbf{0} & 1 \end{bmatrix} \tag{2}$$

The elements of $\mathbf{K}$ include α and β, which represent the scale factors along the x-and-y axes in the image, and γ that is the skew coefficient defining the angle between the x and y axes. The matrix $\mathbf{E}$ represents the rigid transformation that transforms the world frame system to the image frame, composite of a rotation $\mathbf{R} \in \Re^{3\times3}$ and a translation $\vec{T} \in \Re^{3\times1}$.

2.2.1 Radial distortion

Equation 1 does not take into account the lens distortion. Such distortions may be caused by the telecentric lens. The radial distortion is modeled in [31] as:

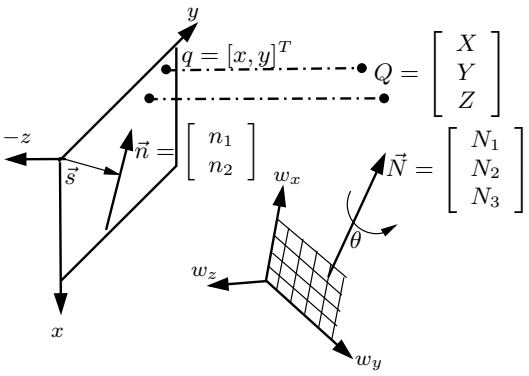

Fig. 4. Rotational reconstruction model. $\vec{N}$ represent the rotation axis and $\vec{n}$ its projection to the image plane.

$$\begin{cases} r^2 = (x - y_0)^2 + (y - y_0)^2 \\ x^d - x_0 = (x - x_0)(1 + l_1 r^2 + l_2 r^4 + \cdots) \\ x^d - y_0 = (y - y_0)(1 + l_1 r^2 + l_2 r^4 + \cdots) \end{cases} \quad (3)$$

where l_1 and l_2 represents the radial distortion, the coordinates (x^d, y^d) are those of the distorted image, (x, y) those of the corrected image and (x_0, y_0) the image center (Figure 3).

2.2.2 Rotation axis

The rotational reconstruction model used in data acquisition is shown in Figure 4. The rotation axis is described by the unit vector $\vec{N} = [N_1, N_2, N_3]^T$ and the translation vector $\vec{s} = [s_1, s_2]^T$ in the camera frame. The image used for object contour dimension is obtained by rotating the object at an angle θ with respect to the rotation axis. Let $Q_i = [X_i, Y_i, Z_i]^T$ be the i points before rotation, respectively; and $q_i = [x_i, y_i]^T$ denotes the corresponding image points. Let $\vec{N}$ be a unit vector along the selected rotation axis and θ be the specified rotation angle around this axis. As shown in [32], the rotation matrix can be written as:

$$\mathbf{M}_R(\theta) = (1 - cos(\theta)) \begin{bmatrix} N_1^2 & N_1N_2 & N_1N_3 \\ N_1N_2 & N_2^2 & N_2N_3 \\ N_1N_3 & N_2N_3 & N_3^2 \end{bmatrix} + \ldots$$
$$\ldots sin(\theta) \begin{bmatrix} 0 & -N_3 & N_2 \\ N_3 & 0 & -N_1 \\ -N_2 & N_1 & 0 \end{bmatrix} + Icos(\theta) \quad (4)$$

The rotation matrix for any rotation axis with a translation vector $\vec{s}$ is expressed as:

$$\mathbf{R}(\theta) = \mathbf{S}^{-1} \begin{bmatrix} \mathbf{M}_R(\theta) & 0 \\ \mathbf{0} & 1 \end{bmatrix} \mathbf{S} \quad (5)$$

where

$$\mathbf{S} = \begin{bmatrix} 1 & 0 & 0 & s_1 \\ 0 & 1 & 0 & s_2 \\ 0 & 0 & 1 & 0 \\ 0 & 0 & 0 & 1 \end{bmatrix}$$

If the rotational axis $\vec{N}$ corresponds to the w_x of the pattern calibration frame, we can compare **E** of Equation 1 with $\mathbf{R}(\theta)$ in Equation 5 ($\mathbf{E} = \mathbf{R}(\theta)$).

However, in Equation 5, if $\vec{N}$ does not correspond to the calibration pattern frame, a rotational matrix and translation vector between rotational axis and pattern frame must be considered (Figure 4), then

$$\mathbf{E} = \begin{bmatrix} \mathbf{R}_{W \leftarrow N} & \vec{T}_{W \leftarrow N} \\ \mathbf{0} & 1 \end{bmatrix} \mathbf{R}(\theta) = \mathbf{E}_{W \leftarrow N} \mathbf{R}(\theta) \quad (6)$$

Equation 1 defines a relationship between image points (q) and world points (Q); if the rotation axis and camera frame are not aligned, this equation can be defined as:

$$q = \mathbf{K}\mathbf{E}_{W \leftarrow N} \mathbf{R}(\theta) Q \quad (7)$$

2.3 Vision system calibration

This section describes a general method to estimate the parameters for the model described in previous section. The model used for estimating the intrinsic and extrinsic parameters separately is presented in [33]. This model uses a multiple images of a standard planar checkerboard pattern. Equation 1 can be written as:

$$q = \begin{bmatrix} \alpha & \gamma & 0 & 0 \\ 0 & \beta & 0 & 0 \\ 0 & 0 & 0 & 1 \end{bmatrix} \begin{bmatrix} r_{11} & r_{12} & r_{13} & t_1 \\ r_{21} & r_{22} & r_{23} & t_2 \\ r_{31} & r_{32} & r_{33} & t_3 \\ 0 & 0 & 0 & 1 \end{bmatrix} \begin{bmatrix} X \\ Y \\ Z \\ 1 \end{bmatrix} \quad (8)$$

The multiplication is carried out, and it is assumed that the calibration pattern is a plane located at $Z = 0$, we have:

$$q = \begin{bmatrix} (\alpha r_{11} + \gamma r_{21})X + (\alpha r_{12} + \gamma r_{22})Y + (\alpha t_1 + \gamma t_2) \\ \beta r_{21} X + \beta r_{22} Y + \beta t_y \\ 1 \end{bmatrix} = \begin{bmatrix} (\alpha r_{11} + \gamma r_{21}) & (\alpha r_{12} + \gamma r_{22}) & (\alpha t_1 + \gamma t_2) \\ \beta r_{21} & +\beta r_{22} & +\beta t_y \\ 0 & 0 & 1 \end{bmatrix} \begin{bmatrix} X \\ Y \\ 1 \end{bmatrix} \quad (9)$$

The last equations can be written as:

$$q = \mathbf{K}_c \mathbf{E}_c \, Q_c$$

$$q = \begin{bmatrix} \alpha & \gamma & 0 \\ 0 & \beta & 0 \\ 0 & 0 & 1 \end{bmatrix} \begin{bmatrix} r_{11} & r_{12} & t_1 \\ r_{21} & r_{22} & t_2 \\ 0 & 0 & 1 \end{bmatrix} \begin{bmatrix} X \\ Y \\ 1 \end{bmatrix} \quad (10)$$

where $\mathbf{R}_c \in \Re^{2\times 2}$ is the truncated rotation matrix and $\vec{T}_c \in \Re^{2\times 1}$ is the truncated translation vector.

The estimation of the intrinsic parameters is obtained from the definition of the homography $\mathbf{H} \in \Re^{3\times 3}$ that relates features of a calibration pattern (e.g., coordinates in the corner of a checkerboard type pattern) with the image, as described in [34].

Substituting Equation 11 in Equation 10 and solving for $\mathbf{H}$, we obtain:

$$q = \mathbf{H} Q_c \quad (11)$$

$$\mathbf{H} = \mathbf{K}_c \mathbf{E}_c \quad (12)$$

Now, multiplying on the left by $\mathbf{K}_c^{-T}$ of Equation 12 ($\mathbf{K}_c^{-1}\mathbf{H} = \mathbf{E}_c$) and subsequently by their respective transposed, the following equation is obtained:

$$\mathbf{E}_c^T \mathbf{E}_c = \mathbf{H}^T \mathbf{K}_c^{-T} \mathbf{K}_c^{-1} \mathbf{H} = \begin{bmatrix} \mathbf{R}_c^T \mathbf{R}_c & \mathbf{R}_c^T \vec{T}_c \\ \vec{T}_c^T \mathbf{R}_c & \vec{T}_c^T \vec{T}_c \end{bmatrix} \quad (13)$$

Equation 13 can be used to solve for the intrinsic parameters, using the upper left submatrix $\mathbf{R}_c^T \mathbf{R}_c$. First, the rotation matrix $\mathbf{R}$ from Equation 2 is expressed in terms of $\mathbf{R}_c$ as follows:

$$\mathbf{R} = \begin{bmatrix} \mathbf{R}_c & \mathbf{B} \\ \mathbf{D}^T & d \end{bmatrix} \quad (14)$$

where $\mathbf{B}, \mathbf{D} \in \Re^{2\times 1}$ y $d \in \Re$. Multiplying both sides of Equation 14 by $\mathbf{R}^T$, we obtain:

$$\mathbf{R}^T \mathbf{R} = \begin{bmatrix} \mathbf{R}_c^T & \mathbf{D} \\ \mathbf{B}^T & d \end{bmatrix} \begin{bmatrix} \mathbf{R}_c & \mathbf{B} \\ \mathbf{D}^T & d \end{bmatrix}$$

$$\mathbf{I}_3 = \begin{bmatrix} \mathbf{R}_c^T \mathbf{R}_c + \mathbf{D}\mathbf{D}^T & \mathbf{R}_c^T \mathbf{B} + \mathbf{D}d \\ \mathbf{B}^T \mathbf{R}_c + d\mathbf{D}^T & \mathbf{B}^T \mathbf{B} + d^2 \end{bmatrix}$$

Extracting the 2x2 upper left sub-matrix, from both sides of the equality, it is obtained:

$$\mathbf{R}_c^T \mathbf{R}_c + \mathbf{D}\mathbf{D}^T = \mathbf{I}_2$$

Features	Value
Dimensions, width x height	$66\ mm \times 52\ mm$
Thickness	$3\ mm$
Active area, width x height	$51\ mm \times 64\ mm$
Cadres, width and spacing	$1.35\ mm$
Dimensional accuracy	$1.9\mu m$

Table 1. Features of the calibration pattern, PT036-056 [7].

$$\mathbf{D}\mathbf{D}^T = \begin{bmatrix} d_{11} \\ d_{21} \end{bmatrix} [d_{11} \quad d_{21}] = \begin{bmatrix} d_{11}^2 & d_{11}\, d_{21} \\ d_{11}\, d_{21} & d_{21}^2 \end{bmatrix}$$

$$det\left(\mathbf{D}\mathbf{D}^T\right) = d_{11}^2\, d_{21}^2 - d_{11}\, d_{21}\, d_{11}\, d_{21} = 0$$

Equation 15 can be defined as follows:

$$det\left(\mathbf{R}_c^T \mathbf{R}_c - \mathbf{I}_2\right) = 0 \quad (15)$$

Expanding Equations 13 and 15 results in:

$$\begin{array}{c} k_1 - k_2\left(h_{21}^2 + h_{22}^2\right) - k_3\left(h_{11}^2 + h_{12}^2\right) + \ldots \\ +2k_4\left(h_{11}h_{21} + h_{12}h_{22}\right) = -\left(h_{12}h_{21} - h_{11}h_{22}\right)^2 \end{array} \quad (16)$$

There will be a homography for each image of the checkerboard pattern, which is defined by:

$$\mathbf{H} = \begin{bmatrix} h_{11} & h_{12} & h_{13} \\ h_{21} & h_{22} & h_{23} \\ h_{31} & h_{32} & h_{33} \end{bmatrix} \quad (17)$$

where $h_{31} = 0$, $h_{32} = 0$ and $h_{33} = 1$. Therefore, if images are taken by the same camera with fixed internal parameters, correspondences between four images are sufficient to recover k_1, k_2, k_3 and k_4, and obtain the intrinsic parameters: α, β and γ.

Finally, the extrinsic parameters $\vec{T}_c$ and $\mathbf{R}_c$ can be found from Equation 12, as described in the next section.

We consider the use of one planar object for calibration. The set of parameters found will project the observed points from 3D world coordinates and the coordinates of the corresponding pixel in the calibration image better. To develop the calibration process, a flat calibration pattern of the checkerboard type (Figure 5) is used. The calibration pattern brand is Opto-Engineering, and its main characteristics are summarized in Table 1.

The process that relates the points position in the pattern with their image position is described in Section 2.2, specifically in Equation 1. The set of process parameters,

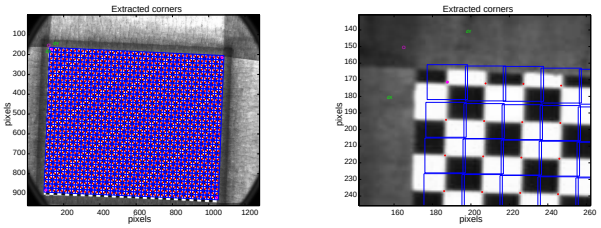

(a) (b)

Fig. 5. Calibration pattern images in grayscale. (a) Corners found in the image of the calibration, (b) the blue boxes indicate the search area of the corner and the red cross is the corner found.

listed below, are unknown: (1) Scale factors: α, β, (2) Skew coefficient: γ, (3) Factors of spatial position: $\mathbf{R}_c$, $\vec{T}_c$, and (4) Radial distortion l_1, l_2. The calibration process refers to estimating a total of 9 scalars that describe the projection of world coordinates in 3D to the image frame. The procedure to obtain these values is developed in 8 steps, as described below:

Step 1: Acquisition of images: capture and storage of n calibration images. In Figure 5, a picture that was used to calibrate the system is observed. The images are in gray scale with a resolution of 1280 x 960 pixels.

Step 1: Acquisition of images
input: Synchronization bit
1. The stage rotates at known angles
2. Delay
3. Camera acquisition
output: I_i, n Calibration images (where $i = 1 \dots n$)

Step 2: Corner extraction with subpixel accuracy. The coordinates correspond to the positions on the checkerboard pattern taking a corner as the origin and from which are measured 1.35 mm intervals $(X_i^j, Y_i^j, 0)$. The coordinates (x_i^j, y_i^j) represent the position in pixels in the image i. Figure 5 shows a detailed view of the square intersections (corners), found in one of the calibration images.

Step 2: Subpixelic corner extraction
input: I_i, n Calibration images
for $i = 1$ **to** n **do**
1.$\{(x_i^j, y_i^j)\} \leftarrow$ SubPixelCornerExtraction(I_i)
2.$\{(X_i^j, Y_i^j, 0)\} \leftarrow$PositionOnCheckerboard($(x_i^j, y_i^j)$)
end
output:$\{(X_i^j, Y_i^j, 0),(x_i^j, y_i^j)\}$, where $j = 1 \dots m$

Step 3: Using calibration images, the homography matrices for each image can be determined using Equations 17 and 11, where the terms h_{11}, h_{12}, h_{13}, h_{21}, h_{22}, and h_{23} are arranged in a vector form in order to establish the equations system as follows:

$$\begin{bmatrix} X_i^1 & Y_i^1 & 1 & 0 & 0 & 0 \\ 0 & 0 & 0 & X_i^1 & Y_i^1 & 1 \\ \vdots & \vdots & \vdots & \vdots & \vdots & \vdots \\ X_i^m & Y_i^m & 1 & 0 & 0 & 0 \\ 0 & 0 & 0 & X_i^m & Y_i^m & 1 \end{bmatrix} \begin{bmatrix} h_{11} \\ h_{12} \\ h_{13} \\ h_{21} \\ h_{22} \\ h_{23} \end{bmatrix} = \begin{bmatrix} x_1^1 \\ y_1^1 \\ \vdots \\ x_i^m \\ y_i^m \end{bmatrix} \quad (18)$$

The value of j is the total number of points by image found in the corner extraction step (step 2). X_i^j and Y_i^j indicate the coordinates of the points in the world frame, x_i^j and y_i^j indicate the coordinates of the points in the image i.

Step 3: Homographies
input:$\{(X_i^j, Y_i^j, 0),(x_i^j, y_i^j)\}$, where $j = 1 \dots m, i = 1, 2, 3, 4$
for $i = 1$ **to** n **do**
$\{h_{11}^i, h_{12}^i, h_{13}^i, h_{21}^i, h_{22}^i, h_{23}^i\} \leftarrow$ Using Equation 18
end
output:$h_{11}^i, h_{12}^i, h_{13}^i, h_{21}^i, h_{22}^i, h_{23}^i$

Step 4: Intrinsic parameters: Using four homographies to compute the first approximation of the intrinsic parameters, the values of h_{11}^i, h_{12}^i, h_{13}^i, h_{21}^i, h_{22}^i, and h_{23}^i solve the equation system $\mathbf{C}\vec{k} = \vec{D}$, which expressed in a matrix form is denoted by Equation 19, for each image i obtained.

$$\begin{bmatrix} C_1^1 & C_2^1 & C_3^1 & C_4^1 \\ C_1^2 & C_2^2 & C_3^2 & C_4^2 \\ C_1^3 & C_2^3 & C_3^3 & C_4^3 \\ C_1^4 & C_2^4 & C_3^4 & C_4^4 \end{bmatrix} \begin{bmatrix} k_1 \\ k_2 \\ k_3 \\ k_4 \end{bmatrix} = \begin{bmatrix} D^1 \\ D^2 \\ D^3 \\ D^4 \end{bmatrix} \quad (19)$$

Now C_1^i, C_2^i, C_3^i, and C_4^i are defined by: $1, -((h_{21}^i)^2 + (h_{22}^i)^2), -((h_{11}^i)^2 + (h_{12}^i)^2), 2(h_{11}^i h_{21}^i + h_{12}^i h_{22}^i)$, where h_{11}^i, h_{12}^i, h_{21}^i, and h_{22}^i corresponds to the value of each homography obtained above (notice that there is one for each i image of the calibration). Moreover, D^i is defined by: $-\left(h_{12}^i h_{21}^i - h_{11}^i h_{22}^i\right)^2$. These definitions correspond to Equation 16. The vector defined by k_1, k_2, k_3, and k_4 represents the necessary scalars to obtain the values of the intrinsic parameters of the camera.

Thus, the values of the camera intrinsic parameters are defined using Equation 19, which allows the calculation of α, β, and γ, scale factors and radial distortion, respectively. These values can be obtained using Equation 20.

$$\alpha = \sqrt{\frac{k_2 k_3 - k_4^2}{k_3}}; \quad \beta = \sqrt{k_3}; \quad \gamma = \sqrt{\frac{k_2 k_3 - k_1}{k_3}} \quad (20)$$

Step 4: Intrinsic parameters

input: $h^i_{11}, h^i_{12}, h^i_{13}, h^i_{21}, h^i_{22}, h^i_{23}$, where $i = 1, 2, 3, 4$

1. $\{k_1, k_2, k_3, k_4\} \leftarrow$ Using Equation 19
2. $\{\alpha, \beta, \gamma\} \leftarrow$ Using Equation 20

output: $\{\alpha, \beta, \gamma\}$

Step 5: Extrinsic parameters require the values of homographies previously obtained: h^i_{11}, h^i_{12}, h^i_{13}, h^i_{21}, h^i_{22} and h^i_{23} complementing **H** homography matrix from Equations 17 and 12. Solving for E_c, we have:

$$\mathbf{E}_c = \begin{bmatrix} \frac{1}{\alpha} & -\frac{\gamma}{\alpha\beta} & 0 \\ 0 & \frac{1}{\beta} & 0 \\ 0 & 0 & 1 \end{bmatrix} \begin{bmatrix} h^i_{11} & h^i_{12} & h^i_{13} \\ h^i_{21} & h^i_{22} & h^i_{23} \\ h^i_{31} & h^i_{32} & h^i_{33} \end{bmatrix}$$

Solving the last equation and using Equation 10, where $\mathbf{E}_c = \begin{bmatrix} r^i_{11} & r^i_{12} & t^i_1 \\ r^i_{21} & r^i_{22} & t^i_2 \\ 0 & 0 & 1 \end{bmatrix}$, we have:

$$\begin{array}{ll} r^i_{11} = \frac{1}{\alpha} h^i_{11} - \frac{1}{\alpha\beta}\gamma h^i_{21} & r^i_{12} = \frac{1}{\alpha} h^i_{12} - \frac{1}{\alpha\beta}\gamma h^i_{22} \\ t^i_1 = \frac{1}{\alpha} h^i_{13} - \frac{1}{\alpha\beta}\gamma h^i_{23} & r^i_{21} = \frac{1}{\beta} h^i_{21} \\ r^i_{22} = \frac{1}{\beta} h^i_{22} & t^i_{21} = \frac{1}{\beta} h^i_{23} \end{array} \quad (21)$$

Step 5: Extrinsic parameters

input: $\{h^i_{11}, h^i_{12}, h^i_{13}, h^i_{21}, h^i_{22}, h^i_{23}\}$, $\{\alpha, \beta, \gamma\}$

for $i = 1$ **to** n **do**

$\{r^i_{11}, r^i_{12}, r^i_{21}, r^i_{22}, t^i_1, t^i_2\} \leftarrow$ Using Equation 21

end

output: $\{r^i_{11}, r^i_{12}, r^i_{21}, r^i_{22}, t^i_1, t^i_2\}$

Step 6: The intrinsic parameters and some extrinsic parameters refinement $(\alpha, \beta, \gamma, \mathbf{R}^i_c, \vec{T}^i_c)$ are now initialized. For the total calibration, Equation 10 is used, and a refinement step is carried out by the total minimization of the following expressions:

$$\begin{array}{l} F_1 = \alpha(r^i_{11}X^j_i + r^i_{12}Y^j_i + t^i_1) + \gamma(r^i_{21}X^j_i + r^i_{22}Y^j_i + t^i_2) - x^j_i \\ F_2 = \beta(r^i_{21}X^j_i + r^i_{22}Y^j_i + t^i_2) - y^j_i \end{array} \quad (22)$$

where (x^j_i, y^j_i) are the pixels measured in the calibration images i. (X^j_i, Y^j_i) are the position of the corner points in the calibration pattern i. The minimisation step uses Matlab implementation of the Levenberg-Marquardt method (LM), and is the minimization obtained by solving the equations system:

$$\frac{\mathrm{d}F_1}{\mathrm{d}\Gamma} = 0; \quad \frac{\mathrm{d}F_2}{\mathrm{d}\Gamma} = 0$$

where $\Gamma = \{\alpha, \gamma, \beta, r^i_{11}, r^i_{12}, r^i_{21}, r^i_{22}, t^i_1, t^i_2\}$, and i correspond to the number of images ($i \gg 4$).

Step 6: Intrinsic and extrinsic parameters refinement

input: $inputParameters = \{\alpha, \beta, \gamma, \mathbf{R}^i_c, \vec{T}^i_c\}$

$inputData = \{(X^j_i, Y^j_i, 0), (x^j_i, y^j_i)\}$

1.$inputParameters \leftarrow LM[F_1, F_2]$

output: $inputParameters$ refinement

Step 7: The intrinsic parameters and some extrinsic parameters refinement $(\alpha, \beta, \gamma, x_0, y_0, l_1, l_2, \mathbf{R}^i_c, \vec{T}^i_c)$ are now initialized. For the total calibration, we use Equation 3.

The minimization uses the Levenberg-Marquardt method of Matlab, and the minimization is computed using the following equations system:

$$\begin{cases} r^2 = (x^j_i - x_0)^2 + (y^j_i - y_0)^2 \\ G_1 = (x^j_i - x_0)(1 + l_1 r^2 + l_2 r^4) + x_0 - (x^j_i)^d \\ G_2 = (y^j_i - y_0)(1 + l_1 r^2 + l_2 r^4) + y_0 - (y^j_i)^d \end{cases} \quad (23)$$

$$\frac{\mathrm{d}G_1}{\mathrm{d}\Gamma} = 0; \quad \frac{\mathrm{d}G_2}{\mathrm{d}\Gamma} = 0$$

where $\Gamma = \{\alpha, \gamma, \beta, x_0, y_0, l_1, l_2, \mathbf{R}^i_c, \vec{T}^i_c\}$, and i corresponds to the number of images (for refinement $i \gg 4$). $((x^j_i)^d, (y^j_i)^d)$ are the pixels measured in the calibration of distorted images are defined by Equation 1.

Step 7: Intrinsic, extrinsic parameters refinement and radial distorsion

input: $inPara = \{\alpha, \gamma, \beta, \mathbf{R}^i_c, \vec{T}^i_c\}$

$inputData = \{(X^j_i, Y^j_i, 0), (x^j_i, y^j_i)\}$

1. $(x_0, y_0) \leftarrow$ image center
2. $l_1 \leftarrow 0$
3. $l_2 \leftarrow 0$
4. $\{inPara, (x_0, y_0), l_1, l_2\} \leftarrow LM[G_1, G_2]$

output: $\{inPara, (x_0, y_0), l_1, l_2\}$

Step 8: In order to calibrate the rotation axis, the calibration pattern is placed on the turntable, for each rotation angle (θ) a matrix $\mathbf{E}(\theta)$ is calculated. In order to calculate $\mathbf{E}_{W \leftarrow N}$, we use the Equation 7.

Step 8: Rotation axis

input: $inPara = \{\alpha, \gamma, \beta, (x_0, y_0), l_1, l_2, \mathbf{R}_c^i, \vec{T}_c^i\}$
$inputData = \{(X_i^j, Y_i^j, 0), (x_i^j, y_i^j)\}$

1. $\theta_i \leftarrow$ read the turntable angle
2. $(s_1, s_2) \leftarrow$ (0,0)
3. $\mathbf{R}_{W\leftarrow N} \leftarrow I_3$
4. $\vec{T}_{W\leftarrow N} \leftarrow [\ 0 \quad 0 \quad 0\ ]^T$
5. **function** rotationAxis($s_1, s_2, \mathbf{R}_{W\leftarrow N}, \vec{T}_{W\leftarrow N}$)
   $\mathbf{R}(\theta) \leftarrow$ Using Equation 5
   $\mathbf{E}_{W\leftarrow N} \leftarrow$ Using Equation 6
   $error \leftarrow q - \mathbf{K}\mathbf{E}_{W\leftarrow N}\mathbf{R}(\theta)Q$
   return $error$
   end function
6. $\{s_1, s_2, \mathbf{R}_{W\leftarrow N}, \vec{T}_{W\leftarrow N}\} \leftarrow LM$(rotationAxis)

output: $\{s_1, s_2, \mathbf{R}_{W\leftarrow N}, \vec{T}_{W\leftarrow N}\}$

3 VISION SYSTEM VALIDATION

Experimental and numerical validations were performed for the vision system. The measurements obtained through the vision system are validated experimentally using a plug gage that is an industrial calibration standard. This experimental validation is performed for the 2D and 3D scenarios. The calibration of the vision system is validated numerically using a Monte Carlo simulation.

3.1 Numerical validation: Camera parameters uncertainty

The uncertainty of the calibration parameters is calculated using Monte Carlo simulation. In [35], a computer-generated random numbers are used to simulate many synthetic data sets. The Monte Carlo method is used for analyzing uncertainty propagation, where the main goal is to determine how random variation, lack of knowledge, or error affect the sensitivity, performance, or reliability of the system that is being modeled. Monte Carlo simulation is categorized as a sampling method because the inputs are randomly generated from probability distributions to simulate the process of sampling from an actual population. The synthetic data set represents the noise of the calibration pattern and it is used to recalculate the parameters of the camera+telecentric lens array $10,000$ times to estimate its uncertainty from the standard deviation. The procedure to evaluate the uncertainty of the camera+telecentric lens array parameters adds noise to ideal coordinates of the reference points for each data acquisition. The noise consists of random numbers with normal probability distribution, zero mean and standard deviation equal to the difference between ideal and real coordinates of the points of reference.

3.2 Experimental validation

The 2D validation projected the points in the image to the world and compared them with the plug gage dimension. The parameters involved in this validation are the intrinsic parameters of the camera. The 3D validation use several images for reconstuction of the plug gage. This validation involves the intrinsic camera parameters and the rotation axis.

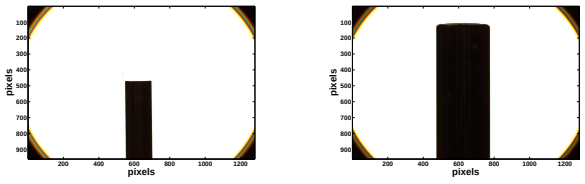

(a) **(b)**

Fig. 6. Plug gage image with dimension **(a)** *10 mm and* **(b)** *20 mm.*

3.2.1 2D performance evaluation

To validate the calibration, a plug gage is used as reference (in world coordinates), with dimension of $5, 10, 16$, and $20\ mm$ with an accuracy of $0.001\ mm$. The procedure consists of computing the distance between the contour points of the plug gage used for measuring from images (Figure 6). The dimension of the plug gage is computed using the Algorithm 1.

Algorithm 1 *Performance evaluation of the proposed measurement system*

Input: plug gage image (Figure 6)

1. Canny edge detector
2. Automatic lines extraction based on the RASAC method.
3. Subpixel extraction points belong to the first line
4. For each subpixel point computed in step 3, we find the subpixel edge point that belongs to the second line and is perpendicular
5. The two subpixels points are projected onto the world frame using the Equation 7
6. The Euclidean distance is computed using the two subpixel points represented in the world

Output: millimetric distance

3.2.2 3D performance evaluation

In this section, we evaluate the uncertainty of the 3D reconstruction. We reconstruct the plug gages in 3D and the measurement are made considered that the plug gage are a cilinders.

In accordance with ISO 14253-1:1998 [36] every measurement process, no matter its nature, must take into account the accuracy represented by a resultant error and its corresponding uncertainty. The uncertainty reported in this work is based on GUM [37] and ISO 15530-3:2011 [38]. The uncertainty expression is given by:

$$U = k \cdot u_c(y) = k \cdot \sqrt{u_{cal}^2 + u_p^2 + u_w^2} + |b| \qquad (24)$$

where: u_{cal} is the uncertainty of calibration standard to be measured, u_p is the standard uncertainty of the sum of errors in the measurement process, and u_w is the standard uncertainty of the material and the manufacture variation. If the systematic error $b = \overline{x} - x_{cal}$ is not corrected after the calibration of the measuring system, it is necessary to take this error b into account. ISO 15530-3:2011 [38] considers that it is more appropriate to calculate the systematic error b arithmetically rather than geometrically.

In [39], the Equation 24 is simplified as follows:

$$U = k \cdot u_p \qquad (25)$$

From Equation 25, the uncertainty u_p is calculated as:

$$u_p = \frac{\sigma_x}{\sqrt{n}} \cdot h \qquad (26)$$

where σ_x is the standard deviation and h is the safety factor calculated on the basis of a student distribution where $h = 1.4$ for $n = 5$ (in our case the plug gage are reconstructed 5 times), in which n is the number of measurements and $h = 1$ for $n >= 10$. k is the coverture factor and in this article a conventional value of 2 was selected to achieve a probability of 94.5% of confidence in the calculated uncertainty.

4 RESULTS

This section describes the conducted experiments and the obtained results used to evaluate the proposed calibration and measurement methods. Finally the implementation of the components proposed for the 3D reconstruction system.

The resolution of the camera Marlin F-145 is 1280 x 960 pixels. The rate of color image acquisition is 10 fps using an IEEE 1394 interface. The gain and exposure time can be set to auto or manual; for these parameters, we used the auto option. The magnification of telecentric lens is 0.074X $\pm$ 3%, the field of view is 65.2×48.9 mm, the work distance is 182.3 ± 5 mm, the maximum typical Telecentricity is 0.06 degrees, and field depth is 124 mm. The motorized Thorlabs Z700 series has a travel range of 360 degrees, gear reduction of 256:1, worm gear of 96 teeth, and a speed range of $6^o/sec$ $22arcsec/sec$. The illumination area of M1000 is 85.6×100.8 mm and the illumination control is 0 to 100 %.

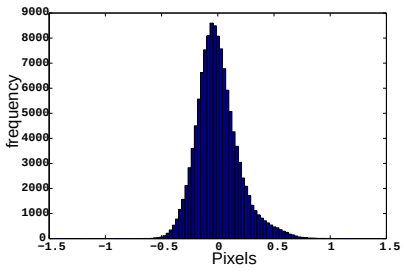

Fig. 7. Histogram of the distance between the re-projected points of the calibration pattern with respect to the points of the calibration images. A total of 61039 points extracted from 54 images are used.

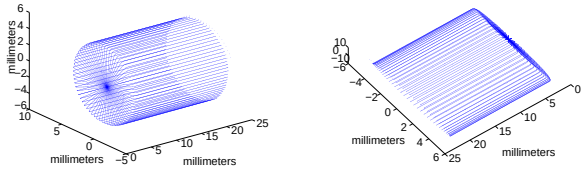

(a) **(b)**

Fig. 8. Two views of the 3D plug gage reconstruction with a dimension of 10 mm.

4.1 Vision system

The calibration of extrinsic and intrinsic camera parameters is done using a checkerboard pattern, as shown in Figure 5. The calibration error and uncertainty of the intrinsic parameters is presented in the following subsections.

4.1.1 Accuracy of the calibration.

To compute α, β, γ of Equation 20 and $\mathbf{H}_c$ used in Equation 17 (**stages** 3, 4, and 5), four images are used. For the intrinsic and extrinsic parameters refinement (**stage** 7), $61,938$ points of 54 calibration images are used. The calibration is carry out by minimizing the residual error. The residual error is calculated using the points of checkerboard pattern re-projected to the images using the final model (Equation 3). The distance between the re-projected point and the extracted image point corresponds to residual error. The histogram of this error is shown in Figure 7. The average error is 0.1358 pixels with a standard deviation of 0.1131 pixels.

To validate the calibration, a plug gages with a dimensions 5, 10, 16, and 20 mm and an uncertainty of 0.002 mm is used as a reference. The vision system acquires images for each plug gage with the turntable in a different orientation. The procedure to validate the calibration

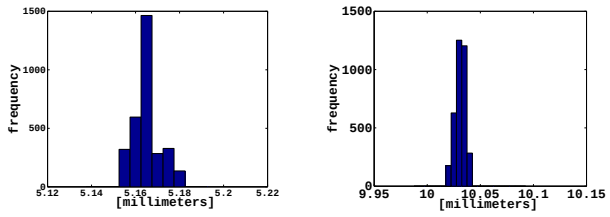

(a) (b)

Fig. 9. Histograms of the distances calculated for the plug gage with dimensions of 5 (a) and 10 (b) millimeters. for each histograms are using 36 images.

Parameters	Computed values	Uncertainty
α(pixel)	15.5231	6.47×10^{-04}
β(pixel)	15.5369	1.11×10^{-04}
γ(pixel)	0.0147	4.79×10^{-04}
l_1	-1.03×10^{-06}	5.0221×10^{-08}
l_2	5.65×10^{-12}	1.7538×10^{-13}

Table 3. Results of the measurement of intrinsic parameters and resulting uncertainties.

is based on measuring the distance between two parallel lines (Algorithm 1) in images. The processing of these images is done by a subpixel edge detection algorithm, and an algorithm to determine the distance (in millimeters) between points of the plug gage image that belongs to the lines. In total, there were 36 measurements at plug gage: 5, 10, 16, and 20 mm. Figure 8 shows a 3D reconstruction of the plug gage with a dimension of 10 mm. Table 2 shows the result of measuring plug gages of different dimensions. Figure 9 shows the distance measurement for the three images for each measurement.

4.1.2 Uncertainty of intrinsic parameters

The uncertainty values reported are in confidence interval of 2σ, which corresponds to a confidence level of 95.4%. The uncertainty values of the intrinsic parameters are given in Table 3.

Table 2 shows the vision system measurements of the plug gages using the computed intrinsic parameters. The second and third column are computed using the technique proposed in section 3.2.1, these measurements are made in 2D and correspond to the plug gage dimensions. The sixth column is computed using the methodology presented in section 3.2.2, measurements of the plug gage are made tridimensionally reconstructing the pattern 5 times and considered it a cilinder, so that the measurements are made in 3D. Adding or subtracting the standard uncertainties to the intrinsic parameters, the measurement are affected by the order of 0.0001 (see Table 4). These results

	Measurement in mm		
Nominal value	Intrinsics parameters (*IP*)	*IP*+ Uc	*IP* - Uc
10	10.0311	10.0310	10.0311
20	19.8381	19.8380	19.8382

Table 4. Measurement of plug gage with dimension 10 and 20 mm using the intrisic paramenters and their uncertainties (Uc). These values are obtained using the algorithm described in section 3.2.1

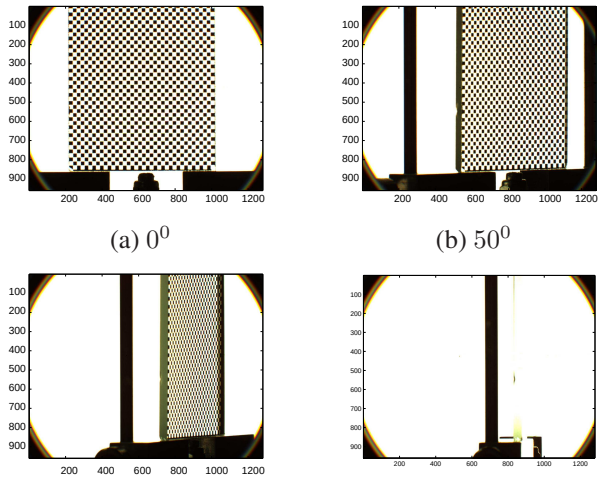

(a) 0^0 (b) 50^0

(c) 75^0 (d) 90^0

Fig. 10. Calibration pattern images acquired at different orientations.

show that the uncertainties of the calibration affects almost negligibly the measurements.

4.2 Rotation axis calibration

For calibration of the rotation axis, the checkerboard is placed on the turntable and images are acquired every five degrees of rotation. Figure 10 shows acquisitions at 0, 25, 50, and 75 degrees.

A total of 73 images were acquired, the pattern orientations are at $1, 5, 10, 15 \ldots 360$ degrees, but there are orientations where it is impossibe to extract points because the plane of the pattern is nearly perpendicular to the image plane (Figures 10 (c) and (d)). For this reason only 54 images were used to calibrate the camera and rotation axis. During the implementation of the vision system, we put attention on the rotation stage to make it coincide with the reference axis of the camera. However, a possible misalignment has been modeled (Equation 10), Figure 11 shows the existing misalignment between the rotation axis and the reference camera. If there are not a misalignments, the values for each orientation in Figure 11 would: $r_{11} = 1, r_{12} = 0, r_{22} = 1, r_{21} = 0$ and $t_1, t_2 = 0$

	Our measure (Section 3.2.1)		Calibration certificate		Uncertainty (Section 3.2.2)
Nominal value (mm)	Average (mm)	Standard deviation (mm)	Average (mm)	Uncertainty (μm)	U (mm)
5	5.0641	0.0059	5.0004	$\pm.2$	0.0060
10	10.0330	0.0052	10.0002	$\pm.2$	0.0069
16	16.0171	0.0201	16.0000	$\pm.2$	0.0630
20	19.9993	0.0217	19.9999	$\pm.2$	0.0700

Table 2. Plug gage with dimension 5, 10, 16, and 20 mm, with an accuracy 0.002 mm used as reference.

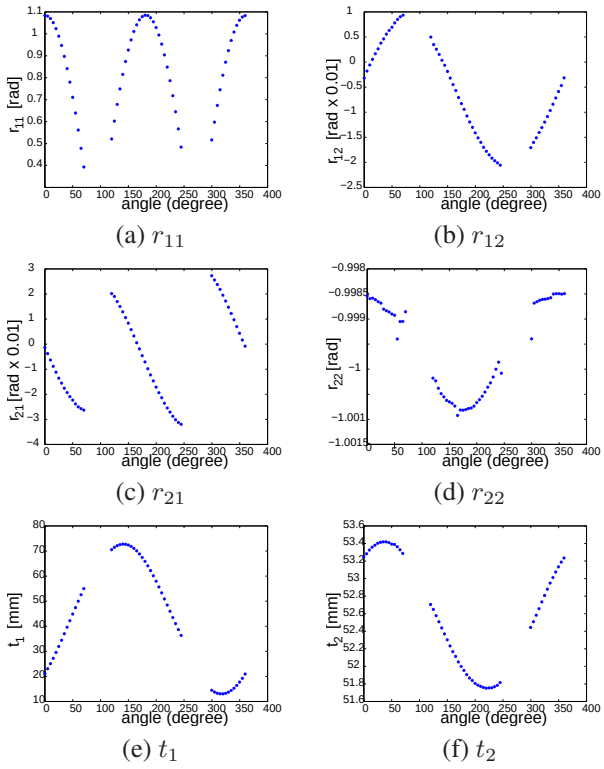

(a) r_{11} (b) r_{12} (c) r_{21} (d) r_{22} (e) t_1 (f) t_2

Fig. 11. Extrinsic parameters with respect to angle of the turn table ($\boldsymbol{E}_c$ of Equation 10)

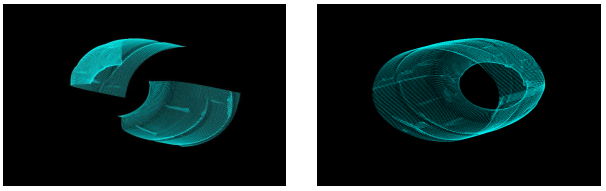

120 silhouettes Final result

Fig. 12. Three-dimensional reconstruction of part of a plastic bottle.

4.3 Three-dimensional reconstruction

In the case of manufactured products, it is important to know and to verify the quality with which they were prepared to comply with the requirements of the product. Therefore, knowing the final product characteristics and quality test results reliably to provide a tool to perform these tests. In particular, it provides the dimensions of the piece and its 3D reconstruction. In this case, a section of an object is reconstructed, using an algorithm that can determine the shape of the object, aligned on an axis of rotation as [40]. It is therefore necessary to know the ratio between the world in millimeters and the world in pixels. This transformation can be found from Equation 7. In this equation Q corresponds to the coordinates in millimeters, and q in pixels. Figure 12 shows the alignment of the silhouettes on a rotation axis, with dimensions in millimeters (area of approximately 50 mm by 45 mm). Also, it shows the process of reconstruction of the object with different silhouettes. Figure 13 presents the results of the final reconstruction of a textured object. Figure 14 (a) shows an object, its 3D reconstruction shown in (b), and the surface mesh is represented in Figure 15.

Figure 16 shows an object with concave zones that cannot be reconstructed with the current method because the contours of these zones are hidden.

5 CONCLUSIONS AND FUTURE WORK

A complete geometric model of an array of camera+telecentric lens has been described. This relates the world coordinates in millimeters to the image coordinates,

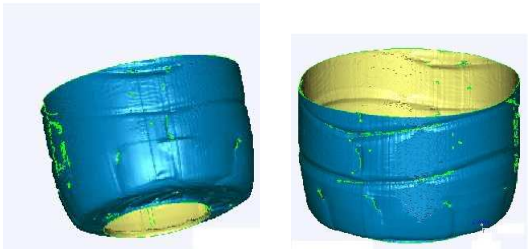

view 1 view 2

Fig. 13. Three-dimensional reconstruction of part of a plastic bottle.

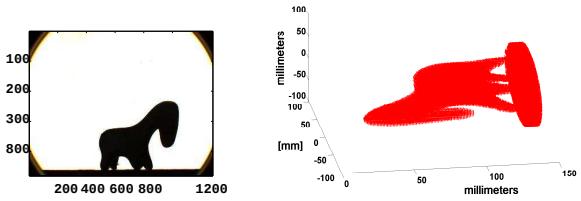

(a) (b)

Fig. 14. Three-dimensional reconstruction of an image of an object: (a) object image (in pixels), (b) 3D points reconstructed.

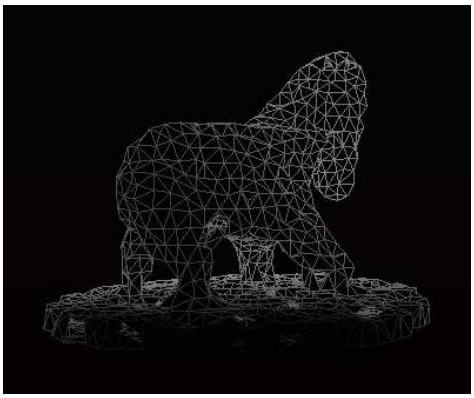

Fig. 15. 3D surface mesh of the object shown in Figure 14.

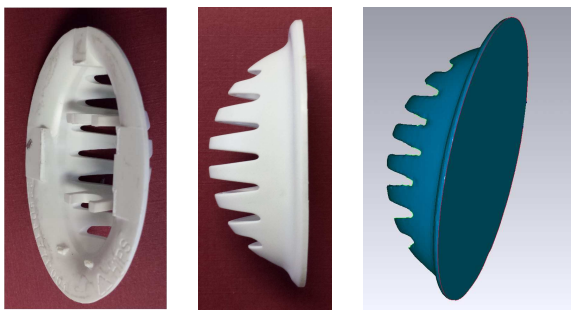

(a) (b) (c)

Fig. 16. (a) and (b) 3D object with concave zones. (c) Reconstruction of 3D object

obtained by the camera, in pixels with high precision and low uncertainty. It also yields the real dimensions from the images. The proposed method determines the dimensions of objects with diameters less than 50 mm.

In this work, we evaluated the accuracy of the 2D measurements and 3D reconstruction between 5 to 20 mm. The accuracy for the measurement in 2D is between ± 0.0059 mm to ± 0.0217 mm. While the accuracy for the 3D reconstruction is between ± 0.006 mm to ± 0.0700 mm. We use plug gages for traceability and correction of the 2D measurements and 3D reconstruction. Several 3D reconstructions are performed to evaluate the performance of the proposed reconstruction system.

The calibration and reconstruction process has been developed using Matlab, but our efforts are aimed at developing algorithms in C++. The future prototype will incorporate a structured light pattern projector in order to reconstruct concave zones that cannot be reconstructed with the current method because the contours of these zones are hidden.

REFERENCES

[1] A. Gallo, M. Muzzupappa, and F. Bruno, "3d reconstruction of small sized objects from a sequence of multi-focused images," *Journal of Cultural Heritage*, 2013.

[2] W. Schweitzer, E. Rohrich, M. Schaepman, M. Thali, and L. Ebert, "Aspects of 3d surface scanner performance for post-mortem skin documentation in forensic medicine using rigid benchmark objects," *Journal of Forensic Radiology and Imaging*, vol. 1, no. 4, pp. 167–175, 2013.

[3] S. Ozan and S. Gumustekin, "Calibration of double stripe 3d laser scanner systems using planarity and orthogonality constraints," *Digital Signal Processing: A Review Journal*, 2013.

[4] J. De Reu, P. De Smedt, D. Herremans, M. Van Meirvenne, P. Laloo, and W. De Clercq, "On introducing an image-based 3d reconstruction method in archaeological excavation practice," *Journal of Archaeological Science*, vol. 41, pp. 251–262, 2014.

[5] M. F. M. Ariff, A. K. Chong, Z. Majid, and H. Setan, "Geometric and radiometric characteristics of a prototype surveillance system," *Measurement*, vol. 46, no. 1, pp. 610 – 620, 2013.

[6] S. Hasinoff and K. Kutulakos, "Confocal stereo," *International Journal of Computer Vision*, vol. 81, no. 1, pp. 82–104, 2009.

[7] O. engineering., "Opto engineering. telecentric lenses tutorial," Enero 2014.

[8] J. Rico Espino, J.-J. Gonzalez-Barbosa, R.-A. Gómez Loenzo, D.-M. Córdova Esparza, and R. Gonzalez-Barbosa, "Vision system for 3d reconstruction with telecentric lens," in *Pattern Recognition* (J. Carrasco-Ochoa, J. Martínez-Trinidad, J. Olvera López, and

K. Boyer, eds.), vol. 7329 of *Lecture Notes in Computer Science*, pp. 127–136, Springer Berlin Heidelberg, 2012.

[9] U. Andersen, D. Pedersen, H. Hansen, and J. Nielsen, "In-process 3d geometry reconstruction of objects produced by direct light projection," *International Journal of Advanced Manufacturing Technology*, pp. 1–9, 2013.

[10] P. Boltryk, M. Hill, J. McBride, and A. Nascè, "A comparison of precision optical displacement sensors for the 3d measurement of complex surface profiles," *Sensors and Actuators, A: Physical*, vol. 142, no. 1, pp. 2–11, 2008.

[11] R. Correal, G. Pajares, and J. Ruz, "Automatic expert system for 3d terrain reconstruction based on stereo vision and histogram matching," *Expert Systems with Applications*, p. 2043–2051, 2014.

[12] R. Lati, S. Filin, and H. Eizenberg, "Estimating plant growth parameters using an energy minimization-based stereovision model," *Computers and Electronics in Agriculture*, vol. 98, pp. 260–271, 2013.

[13] C. Daul, J. Lopez-Hernandez, D. Wolf, G. Karcher, and G. Ethévenot, "3-d multimodal cardiac data superimposition using 2-d image registration and 3-d reconstruction from multiple views," *Image and Vision Computing*, vol. 27, no. 6, pp. 790–802, 2009.

[14] J. Smeeckaert, C. Mallet, N. David, N. Chehata, and A. Ferraz, "Large-scale classification of water areas using airborne topographic lidar data," *Remote Sensing of Environment*, vol. 138, pp. 134–148, 2013.

[15] C. Tian, M. Masry, and H. Lipson, "Physical sketching: Reconstruction and analysis of 3d objects from freehand sketches," *CAD Computer Aided Design*, vol. 41, no. 3, pp. 147–158, 2009.

[16] J. Adam, M. Klinkmuller, G. Schreurs, and B. Wieneke, "Quantitative 3d strain analysis in analogue experiments simulating tectonic deformation: Integration of x-ray computed tomography and digital volume correlation techniques," *Journal of Structural Geology*, vol. 55, pp. 127–149, 2013.

[17] I. Garcia-Dorado, I. Demir, and D. Aliaga, "Automatic urban modeling using volumetric reconstruction with surface graph cuts," *Computers and Graphics (Pergamon)*, vol. 37, no. 7, pp. 896–910, 2013.

[18] M. Toda and K. Grabowska, "Computed microtomography in the analysis of fiber migration in yarn," *Autex Research Journal*, vol. 13, no. 1, pp. 28–32, 2013.

[19] E. Stanfield, B. Muralikrishnan, T. Doiron, A. Zheng, S. Orandi, and D. Duquette, "Two applications of small feature dimensional measurements on a coordinate measuring machine with a fiber probe," *Measurement Science and Technology*, vol. 24, no. 10, 2013.

[20] I.-B. Kong and S.-W. Kim, "Portable inspection of precision surfaces by phase-shifting interferometry with automatic suppression of phase-shift errors," *Optical Engineering*, vol. 34, no. 5, pp. 1400–1404, 1995.

[21] S. Seitz, B. Curless, J. Diebel, D. Scharstein, and R. Szeliski, "A comparison and evaluation of multi-view stereo reconstruction algorithms," in *Computer Vision and Pattern Recognition, 2006 IEEE Computer Society Conference on*, vol. 1, pp. 519–528, June 2006.

[22] K. Potsch and A. Pinz, "3d geometric shape modeling by 3d contour cloud reconstruction from stereo videos," in *Proceedings of the Computer Vision Winter Workshop*, CVWW '04, pp. 429–436, Andreas Wendel, Sabine Sternig, Martin Godec, 2011.

[23] D. Gorpas, K. Politopoulos, and D. Yova, "A binocular machine vision system for three-dimensional surface measurement of small objects," *Comp. Med. Imag. and Graph.*, vol. 31, no. 8, pp. 625–637, 2007.

[24] M.-F. R. Lee, C. W. de Silva, E. A. Croft, and Q. J. Wu, "Machine vision system for curved surface inspection," *Machine Vision and Applications*, vol. 12, no. 4, pp. 177–188, 2000.

[25] E. Guerra and J. R. Villalobos, "A three-dimensional automated visual inspection system for smt assembly," *Comput. Ind. Eng.*, vol. 40, pp. 175–190, June 2001.

[26] D. Langer, M. Mettenleiter, F. Härtl, and C. Fröhlich, "Imaging laser scanners for 3-d modeling and surveying applications," *Proceedings of the 2000 IEEE International Conference on Robotics and Automation*, vol. 1, pp. 116 – 121, 2000.

[27] J. Leopold, H. Günther, and R. Leopold, "New developments in fast 3d-surface quality control," *Measurement*, vol. 33, no. 2, pp. 179 – 187, 2003. {IMEKO} {WORLD} {CONGRESS} (VIENNA).

[28] M. Toyoura, M. Iiyama, T. Funatomi, K. Kakusho, and M. Minoh, "3d shape reconstruction from incomplete silhouettes in multiple frames," in *Pattern Recognition, 2008. ICPR 2008. 19th International Conference on*, pp. 1–4, Dec 2008.

[29] D. Li and J. Tian, "An accurate calibration method for a camera with telecentric lenses," *Optics and Lasers in Engineering*, vol. 51, no. 5, pp. 538 – 541, 2013aa.

[30] Y. Liu, H. Pottmann, and W. Wang, "Constrained 3d shape reconstruction using a combination of surface fitting and registration," *Comput. Aided Des.*, vol. 38, pp. 572–583, June 2006.

[31] M. Devy, V. Garric, and J. Orteu, "Camera calibration from multiple views of a 2d object, using a global non linear minimization method," in *IEEE International Conference on Intelligent Robots and Systems*, vol. 3, pp. 1583–1589, 1997.

[32] E. Trucco and A. Verri, *Introductory Techniques for 3-D Computer Vision*. Upper Saddle River, NJ, USA: Prentice Hall PTR, 1998.

[33] D. Lanman, D. Hauagge, and G. Taubin, "Shape from depth discontinuities under orthographic projection," in *Computer Vision Workshops (ICCV Workshops), 2009 IEEE 12th International Conference on*, pp. 1550–1557, Sept 2009.

[34] Z. Zhang, "Flexible camera calibration by viewing a plane from unknown orientations," *Computer Vision, The Proceedings of the Seventh IEEE International Conference on*, vol. 1, pp. 666–673, 1999.

[35] W. H. Press, S. A. Teukolsky, W. T. Vetterling, and B. P. Flannery, *Numerical recipes in C (2nd ed.): the art of scientific computing*. New York, NY, USA: Cambridge University Press, 1992.

[36] I. 2011, "Geometrical Product Specification (GPS). Inspection by measurement of workpieces and measuring equipment – Part 1: Decision rules for proving conformance or non-conformance with specification," 1998.

[37] JCGM, "Evaluation of measurement data — Guide to the expression of uncertainty in measurement," tech. rep., Joint Committee for Guides in Metrology (JCGM), 2008.

[38] "Geometrical Product Specification (GPS).Coordinate Measuring Machines (CMM): Technique for Determining the Uncertainty of Measurement—Part 3 ," 2011.

[39] O. Icasio-Hernández, J.-J. Gonzalez-Barbosa, and J.-B. H.-R. amd M. Viliesid-Alonso, "3d reconstruction oh hollow parts analysing images acquired by a fiberscope," *Measurement Science and Technology*, vol. 25, no. 7, p. 075402, 2014.

[40] G. Taubin, D. Crispell, D. Lanman, P. Sibley, and Y. Zhao, "Shape from depth discontinuities," in *Emerging Trends in Visual Computing* (F. Nielsen, ed.), (Berlin, Heidelberg), pp. 216–237, Springer-Verlag, 2009.

José-Joel Gonzalez-Barbosa He received the M.S. degree in Electrical Engineering from the University of Guanajuato, Mexico in 1998, and Ph.D. degree in Computer Science and Telecommunications from National Polytechnic Institute of Toulouse, France in 2004. He is an Associate Professor at the CICATA Querétaro-IPN, Mexico, where he teaches courses in Computer Vision and Image Processing. His current research interests include perception and mobile robotics.

José-Guadalupe Rico-Espino received the B. Eng. Degree in Electronic Engineering from ITQ, Mexico in 2003, the MsC degree in Control of Process and Instrumentation, from UAQ, México in 2011. He is currently working in CIATEQ, Mexico for the area of Mechanical Systems in projects related to the application of image processing techniques and automated testing equipment for evaluating the performance of home appliances within the field of fluid dynamics.

Roberto-Augusto Gómez-Loenzo received MS in Automation and Control from the Universidad Autónoma de Querétaro in 2007 and PhD in Engineering in 2011. Since then he is a professor and researcher at the same university and maintains a level 1 SNI awarded by CONACyT. Interests include computer and CNC machine programming.

Hugo Jiménez-Hernández is a titular professor researcher at the CIDESI. He received his BS in computer science, in Institute Technological of Querétaro, México, MS degrees in Computer Science and Ph. D in Computer Vision, at Politechnical Institute of México. He is the author of more than 15 journal papers. His current research interests include Computer Vision, Visual Inference, and Computer Theory.

Miguel Razo is a CS Faculty at The University of Texas at Dallas. He obtained his Ph.D. in Computer Science in 2009.His research interests include telecommunication software design, network planning and optimization algorithms.

Ricardo Gonzalez-Barbosa is a Research Professor in the Departmen of Environmental Engineering at Guanajuato University in Division of Life Sciences

AUTHORS' ADDRESSES

Assoc. Prof. José-Joel Gonzalez-Barbosa
Instituto Politécnico Nacional
CICATA Querétaro
Cerro Blanco No. 141, Col Colinas del Cimatario,
Querétaro, Qro, México C.P. 76090
email: jgonzalezba@ipn.mx

Development Engineer José-Guadalupe Rico-Espino
CIATEQ, Advanced Technology Center

Assoc. Prof. Roberto-Augusto Gómez-Loenzo
Universidad Autónoma de Querétaro, México

Assoc. Prof. Hugo Jiménez-Hernández
CIDESI, Centro de Investigación e Ingeniería Industrial.

Senior lecturer Miguel Razo
Erik Jonsson School of Engineering and Computer Science
University of Texas at Dallas

Assoc. Prof. Ricardo Gonzalez-Barbosa
División Ciencias de la Vida, Universidad de Guanajuato,

Received: 2014-10-03
Accepted: 2015-02-25